





Computational investigation of flow dynamics and mechanical retention of age-associated red blood cells in the spleen

Shuhao Ma , Xiaojing Qi, Keqin Han, Shuo Wang , Guoqing Hu ,* and Xuejin Li [†]
State Key Laboratory of Fluid Power and Mechatronic Systems, Department of Engineering Mechanics, and Center for X-Mechanics, Zhejiang University, Hangzhou 310027, People's Republic of China



(Received 12 August 2022; accepted 2 June 2023; published 21 June 2023)

Red blood cells (RBCs) change shape and deformability with age, making them more likely to be trapped in the splenic slits (IESs) and removed from circulation. Existing evidence suggests that cell size and viscoelastic properties are altered during aging, making it challenging to identify the determinants of mechanical retention of aged RBCs in the spleen. Herein, we present a comprehensive computational study to investigate the flow dynamics, morphological changes, and mechanical retention of age-associated RBCs in the splenic IESs. Our results show that, before reaching the critical size for the age-associated RBC to be trapped in the IESs, the reduced size of the RBC can shorten the transit time it takes to pass through the IESs, while the increased membrane viscosity slows it down. A narrower IES requires the RBC to undergo greater deformation to pass through. Furthermore, during the shrinkage associated with normal aging, a more significant critical pressure gradient is required for RBCs to deform more to pass through the IESs, resulting in more intense damage. These quantitative findings provide unique insights into the traversal dynamics and retention mechanism of age-associated RBCs.

DOI: [10.1103/PhysRevFluids.8.063103](https://doi.org/10.1103/PhysRevFluids.8.063103)

I. INTRODUCTION

The spleen, located in the upper left abdomen, is the largest organ for secondary immunity, accounting for about 25% of the total lymphatic tissue of the entire human body [1,2]. The cellular and humoral immunity centers contain many lymphocytes and macrophages, which can help eliminate pathogens and abnormal red blood cells (RBCs) to protect the body from pathogenic microorganisms and blood diseases. Blood entering the spleen flows through two functionally distinct compartments, the white and red pulps. The former, mainly composed of lymphoid tissue, identify blood-borne antigens and initiates the appropriate immune response. The red pulp, on the other hand, acts as a blood filter. The primary filtering holes are the interendothelial slits (IESs) formed by the endothelial cells and annular fibers that allow healthy RBCs to pass through after undergoing extreme deformation [see Figs. 1(a)–1(c)]. However, unhealthy, old, or misshapen RBCs are often unable to pass through this passage and are retained and removed from the bloodstream.

Mature RBCs are produced from hematopoietic stem cells via a series of differentiations and cleared by the spleen after roughly 120 days under normal circumstances. A young mature, healthy RBC is a nuclear-less biconcave-shaped cell with a diameter of about $7.8\ \mu\text{m}$ and a thickness of about $2\ \mu\text{m}$. Such a unique structure enables the RBCs to pass through narrow capillaries of $3\ \mu\text{m}$ diameter and splenic IESs down to $0.6\ \mu\text{m}$ wide. Cyclic deformation through significant elastic stretching and relaxation as the RBCs circulate in the bloodstream causes cumulative fatigue

*ghu@zju.edu.cn

[†]xuejin_li@zju.edu.cn

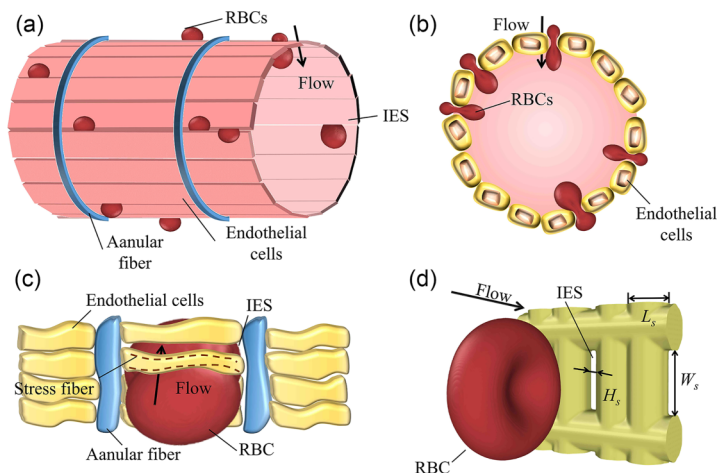


FIG. 1. Schematic representation of the traversal process of individual RBCs through the splenic IESs. Note that the schematics (a) and (b) are adapted from Refs. [1] and [3], respectively.

damage, leading to alterations in cell deformability and membrane viscoelasticity [4–9]. These altered RBCs would be intercepted and cleared in the spleen because they cannot perform their physiological functions properly [10].

Limited by ethics and observational resources, it is a challenge to detect the mechanics and dynamics of RBC passage through the splenic IESs in the human body. The only treasure trove of *in vivo* data and images comes from experimental rat models by MacDonald *et al.* [11,12], who investigated the kinetics of RBC passage through the rat splenic IESs. In addition, Safeukui *et al.* developed an *ex vivo* perfusion of the human spleen system to explore the retention kinetics of the surface-altered RBCs [13,14]. They showed that the RBCs with reduced surface area-to-volume (S_A/V) ratio (or increased cell sphericity) would be entrapped by the splenic IESs. In contrast, those with reduced cell membrane deformability do not significantly reduce their ability to cross the splenic IESs. Microfluidics, which allows for precise control of the mechanical and chemical environment around the living cells, has emerged as a powerful enabling technology for investigating cell behavior from the single cell to the multicellular level. In the past decades, many researchers have paid attention to the passage of RBCs through narrow spaces with diameters smaller than the cell size [13–21]. For example, Quinn *et al.* investigated the biophysical properties of healthy RBCs traversing microfluidic channels with cross-sectional areas as small as $2.7\ \mu\text{m} \times 3\ \mu\text{m}$ [15]. They identified a cross-sectional area threshold below which the RBC membrane characteristics begin to dominate its flow dynamic behavior at room temperature. Picot *et al.* employed a spleen-like microfluidic device to study the flow behavior and mechanical retention of the RBCs in the splenic IESs [17]. They showed that the RBCs with a low S_A/V ratio are more prone to trapping in the splenic IESs, indicating that the S_A/V ratio plays a vital role in the mechanical clearance of RBCs by the spleen. In a recent study, Qiang *et al.* developed a spleen-on-a-chip platform to study splenic retention and RBC elimination [21]. They showed that the retention of sickle RBCs in spleen-like IESs increases significantly under normoxia and even more intensely under hypoxia than normal RBCs. The capabilities of the microfluidic technology also allow the study of the mechanical fatigue and aging of RBCs caused by cyclic mechanical deformation as they recirculate through the spleen during their 120-day lifespan [13,16,20,22–24]. For example, Sakuma *et al.* [16] and Qiang *et al.* [24] show that cyclic straining of RBCs, caused either by passing through IES-like microfluidic constrictions or by amplitude-modulated electrodeformation, leads to significant changes in the mechanical properties of the RBCs. Recently, Garcia-Herreros *et al.* demonstrated that cyclic passage through IES-like microfluidic constrictions affects the mechanical properties and molecular

composition of RBCs, thereby accelerating cell aging [20]. These results provide unique insights into how cyclic mechanical stress induces RBC clearance in the spleen.

In addition to the experimental studies mentioned above, recent advances in computational modeling and simulation allow the investigation of the flow of microcirculatory blood flow dynamics [15,25–34] and splenic blood flow [35–42]. For example, Freund employed a boundary integral model (BIM) to study the flow dynamics of a RBC through a spleen-like IES [35]. They observed that the old RBC with elevated cytosol viscosity slows the RBC passage through the splenic IES compared with a young, healthy one. Pivkin *et al.* performed a computational study to simulate RBC passage through the splenic IESs [37]. They showed that the S_A/V ratio of the RBC is a more critical determinant of splenic IES retention than its membrane stiffness, which agrees with previous experimental results [13].

These experimental and computational studies have helped us better understand the process of splenic IES clearance of RBCs. However, the mechanism underlying the traversal dynamics of the interception of age-associated RBCs in the splenic IESs remains unclear. On the one hand, previous experimental and computational studies have shown that the altered RBC membrane stiffness does not significantly contribute to the mechanical retention of RBCs in the spleen [14,37,39,43]. However, the effect of surface-altered membrane viscosity during cell aging, an important factor affecting cell rheology and dynamics [44–51], on cell passage in the spleen has not been systematically investigated in previous studies. On the other hand, some available experiments evince that the S_A/V ratio of RBCs may not reduce during their aging processes [4,52,53]. In contrast, most previous studies on splenic IES retention of RBCs did not consider that the surface area and volume of age-associated RBCs are decreased compared with those of young mature ones [37,39,42,43]. The above facts obscure the reasons for the interception of age-associated RBCs in spleen IESs.

It is known that several biophysical factors (including cell size, cell stiffness, and cell membrane viscosity) and external environmental factors (such as cell orientation and its relative position to the slit) can influence the process of cell transit through splenic IESs. However, *in vitro* experimental measurements have limitations in isolating different factors for study and, like other experimental studies, have variable control problems. In contrast, the computational approach can isolate the role of each factor in the RBC passage. In this study, we perform detailed computational simulations by applying the dissipative particle dynamics–based (DPD-based) mesoscopic RBC model to study the flow dynamics and mechanical retention of the age-associated RBCs in the splenic IESs. Specifically, we focus on the isolated effects of cell size and viscoelastic properties of the age-associated RBCs and their combined effects on the changes in their passage through the splenic IESs with different slit opening widths. In the remainder of this article, we first briefly review the DPD method and the DPD-based mesoscopic RBC model. Then, we present and discuss our simulation results in detail. Finally, we summarize the main results and draw a conclusion.

II. MODELS AND METHODS

In this work, we study the flow dynamics of age-associated RBCs crossing the splenic IESs with the help of the DPD-based mesoscopic RBC model. The splenic IES is modeled as a rigid structure with several vertical and horizontal bars [Fig. 1(d)]. The fluids, including cytosol and extracellular fluid, are established as free DPD particles with number density of 1 and 3, respectively. And impermeable and no-slip boundary conditions are applied at the fluid-solid boundary through bounce-back reflections and proper dissipative forces. Each DPD particle interacts with other particles through pairwise DPD forces. This section briefly reviews the DPD method and the DPD-based mesoscopic RBC model. For more details on the RBC model, we refer to Refs. [54,55].

A. Dissipative particle dynamics method

Dissipative particle dynamics is a coarse-grained mesoscopic method in which each DPD particle is regarded as a lump of molecules. Within the cutoff radius r_c , each particle i interacts with a

surrounding particle j by three pairwise forces, including a conservative force \mathbf{F}_{ij}^C , a dissipative force \mathbf{F}_{ij}^D , and a random force \mathbf{F}_{ij}^R , as

$$\mathbf{F}_i^{\text{DPD}} = \sum_{j \neq i} (\mathbf{F}_{ij}^C + \mathbf{F}_{ij}^D + \mathbf{F}_{ij}^R), \quad r_{ij} \leq r_c, \quad (1)$$

$$\mathbf{F}_{ij}^C = a_{ij} \omega(r_{ij}) \mathbf{e}_{ij}, \quad (2)$$

$$\mathbf{F}_{ij}^D = -\gamma \omega^2(r_{ij}) (\mathbf{e}_{ij} \cdot \mathbf{v}_{ij}) \mathbf{e}_{ij}, \quad (3)$$

$$\mathbf{F}_{ij}^R = \sigma \omega(r_{ij}) \xi_{ij} \Delta t^{-1/2} \mathbf{e}_{ij}, \quad (4)$$

where r_{ij} and \mathbf{v}_{ij} are, respectively, the distance and the relative velocity between particles i and j , \mathbf{e}_{ij} is the unit direction vector between these two interacting particles, a_{ij} is the conservative force coefficient, ξ_{ij} is a Gaussian random number with zero mean and unit variance, Δt is the time-step size, γ is the dissipative force coefficient. The random force coefficient $\sigma = \sqrt{2\gamma k_B T}$, where k_B and T are the Boltzmann constant and temperature. The weight function $\omega(r_{ij})$ is set as follows:

$$\omega(r_{ij}) = \begin{cases} (1 - r_{ij}/r_c)^s & r_{ij} \leq r_c \\ 0 & r_{ij} > r_c, \end{cases} \quad (5)$$

where s denotes the exponent of the weight function.

B. Dissipative particle dynamics–based mesoscopic red blood cell model

The RBC membrane is modeled as a two-dimensional triangulated network composed of N_t triangles, which contain N_v DPD particles and N_s bonds as vertices and edges of the triangles, respectively. The total potential energy of the RBC membrane system is defined as four parts,

$$U = U_{\text{in-plane}} + U_{\text{bending}} + U_{\text{area}} + U_{\text{volume}}. \quad (6)$$

The in-plane elastic part is taken as

$$U_{\text{in-plane}} = \sum_{j \in 1 \dots N_s} \left[\frac{k_B T l_m (3x_j^2 - 2x_j^3)}{4p(1-x_j)} + \frac{k_p}{(v-1)l_j^{v-1}} \right], \quad (7)$$

where l_j is the equilibrium length of the edge j , l_m is its maximum extension, $x_j = l_j/l_m$, p is the persistence length, k_p is the spring constant, and v is a specified exponent. By following the theoretical analysis for a regular hexagonal network by Dao *et al.* [56], the membrane shear modulus can be calculated as

$$\mu = \frac{\sqrt{3}k_B T}{4pl_m x_0} \left[\frac{x_0}{2(1-x_0)^3} - \frac{1}{4(1-x_0)^2} + \frac{1}{4} \right] + \frac{\sqrt{3}k_p(v+1)}{4l_0^v + 1}, \quad (8)$$

where l_0 is the equilibrium length of spring and $x_0 = l_0/l_m$.

The bending energy of the RBC membrane is given by

$$U_{\text{bending}} = \sum_{j \in 1 \dots N_s} k_b [1 - \cos(\theta_j - \theta_0)], \quad (9)$$

where k_b is the bending constant, θ_j is the instantaneous angle between two adjacent triangles sharing the same edge j , and θ_0 is the spontaneous angle. For a macroscopic bending model with zero in-plane shear modulus, the bending rigidity k_c of the Helfrich model is calculated to be $\sqrt{3}k_b/2$.

The elastic energy of the surface area and volume of the RBC is introduced to constrain the membrane deformation and cytosol compressibility, given by

$$U_{\text{area}} = \frac{k_a(S_A - S_{A,0})^2}{2S_{A,0}} + \sum_{j \in 1 \dots N_i} \frac{k_d(A_j - A_{j,0})^2}{2A_{j,0}}, \quad (10)$$

$$U_{\text{volume}} = \frac{k_v(V - V_0)^2}{2V_0}, \quad (11)$$

where k_d , k_a , and k_v , are the constraint coefficients of the local area, global area, and volume, respectively. $A_{j,0}$, $S_{A,0}$, and V_0 are the area of triangle j , the surface area, and the total volume of the RBC at the stress-free state, respectively.

The area-compression modulus (K) and Young's modulus (Y) of the RBC membrane can be respectively calculated as

$$K = 2\mu + k_a + k_d, \quad (12)$$

$$Y = \frac{4K\mu}{K + \mu}, \quad (13)$$

The membrane viscosity is imposed by introducing dissipative force and random force on each spring instead of Eqs. (3) and (4), which follows the framework proposed by Español [57],

$$\mathbf{F}_{ij}^D = -\gamma^T \mathbf{v}_{ij} - \gamma^C (\mathbf{v}_{ij} \times \mathbf{e}_{ij}) \mathbf{e}_{ij}, \quad (14)$$

$$\mathbf{F}_{ij}^R dt = \sqrt{2k_B T} \left(\sqrt{2\gamma^T} d\overline{\mathbf{W}}_{ij}^S + \sqrt{3\gamma^C - \gamma^T} \frac{\text{tr}[d\mathbf{W}_{ij}]}{3} \mathbf{1} \right) \times \mathbf{e}_{ij}, \quad (15)$$

where γ^T and γ^C are dissipative parameters, \mathbf{v}_{ij} is the relative velocity of spring ends, $d\overline{\mathbf{W}}_{ij}^S$ is the trace-less symmetric part of a random matrix of independent Wiener increments $d\mathbf{W}_{ij}$, and tr represents the trace of the matrix. Following the analysis by Fedosov *et al.* [55], other dissipative and random forces are excluded in the RBC model so that the membrane viscosity can be determined by

$$\eta_m = \sqrt{3}\gamma^T + \frac{\sqrt{3}}{4}\gamma^C. \quad (16)$$

According to the research of Liu *et al.* [58], the viscosity of the interior fluid is estimated as

$$\eta_i = \frac{2\pi\gamma\rho_i^2 r_c^5}{15} \left(\frac{1}{s+1} - \frac{4}{s+2} + \frac{6}{s+3} - \frac{4}{s+4} + \frac{1}{s+5} \right), \quad (17)$$

where ρ_i is the number density of internal fluid particles.

Following the mapping strategy by Pivkin *et al.* [54] and Fedosov *et al.* [55], we obtain the DPD length, energy, and timescales, as $l_{\text{scale}} = d_R^P/d_R^M \approx 0.3128 \mu\text{m}$, $E_{\text{scale}} = (k_B T)^P/(k_B T)^M \approx 1.07 \times 10^{-19} \text{J}$, $\tau_{\text{scale}} = \eta_m^P \mu^M / \eta_m^M \mu^P \approx 0.864 \text{ms}$, where d_R and η are diameter and membrane viscosity of RBC, superscript P and M represent parameter values in the physical and model units, respectively.

C. Parameter estimation and model setup

Physiologically, a young normal human RBC has a biconcave shape with a large S_A/V ratio, which supports the remarkable deformation that occurs as it circulates in the blood. During the 120-day lifespan of a human RBC, cyclic strain loading accumulates mechanical damage to the cell membrane, causing a reduced cell volume and local densification of the spectrin network. In this study, the RBC model composed of $N_v = 23867$ particles is used; each DPD particle represents a junctional complex in the spectrin network of the RBC membrane and each spring in the network

TABLE I. Geometric parameters of different sizes of RBCs. The symbol RBC-I represents a young, healthy RBC with typical cell volume and surface area values. In contrast, the RBC-II and RBC-III represent senescent RBCs with reduced cell volume and surface area. The $S_{A,0}/V_0$ of RBC-II is maintained to be the same as RBC-I, while the volume of RBC-III is the same as RBC-II but with a smaller $S_{A,0}/V_0$.

	$S_{A,0}$ (μm^2)	V_0 (μm^3)	$S_{A,0}/V_0$ (μm^{-1})	SI
RBC-I	134.0	94.0	1.425	0.746
RBC-II	111.2	78.0	1.425	0.794
RBC-III	100.1	78.0	1.283	0.882

corresponds to a single spectrin tetramer with an equilibrium distance between two adjacent actin junctions of about 75 nm. For more efficient simulations, the RBC network can also be highly coarse-grained with the equilibrium spring length of up to 500 nm. We also consider a coarser RBC model with $N_v = 9128$ and a finer RBC model with $N_v = 27344$ to investigate the influence of N_v on RBC shrinkage and slit flow, shown in the Supplemental Material [59]. Considering that the senescent RBCs would have reduced surface area and volume values [20,52,53], we apply three different sizes of RBCs, as shown in Table I, to simulate the shrinkage of RBCs under cell aging. For details, the size of the RBC-I is set to be $S_{A,0} = 134 \mu\text{m}^2$ and $V_0 = 94 \mu\text{m}^3$, which is regarded as a normal young RBC. The volume of RBC-II is set to about 83% of the former and its $S_{A,0}/V_0$ ratio is kept in line with RBC-I, namely $S_{A,0}/V_0 = 1.425 \mu\text{m}^{-1}$. However, the sphericity index, $\text{SI} = \pi^{1/3} 6^{2/3} V^{2/3} / S_A$, of the RBC-II is about 0.794, which is larger than that of the RBC-I (0.746). Furthermore, the volume of RBC-III is set to have the same volume as RBC-II, but a decreased $S_{A,0}/V_0 = 1.283 \mu\text{m}^{-1}$, and the SI is calculated to be 0.882. Additionally, several experimental and computational studies have shown that the dense spectrin network of age-associated RBCs significantly escalates the shear modulus and membrane viscosity values compared with young mature RBCs [5]. In our previous study, we developed a multiscale computational framework for RBC modeling to predict the viscoelastic properties of age-associated RBCs [45], which can serve as a guide for the model setup of the present study (Table II). The shear modulus and membrane viscosity of young healthy RBCs ($n = 0\%$, where n denotes the increment of spectrin network connectivity compared with young RBCs, see Supplemental Material for definition [59]) are $\mu = 10.3 \mu\text{N/m}$ and $\eta_m = 0.46 \mu\text{N/ms}$, respectively, both of which fall within the normal range obtained by experimental measurement of about $\mu = 4\text{--}12 \mu\text{N/m}$ [22,24,60–63] and $\eta_m = 0.057\text{--}2.8 \mu\text{N/ms}$ [22,24,60–62,64–66]. The shear modulus of the cell membrane increases linearly with n while the membrane viscosity grows exponentially, see Table II. Other key parameters of the model RBCs are set as $\eta_i = 6 \text{ cP}$ and $k_c = 2.1 \times 10^{-19} \text{ J}$.

In the spleen, endothelial cells are connected by annular stress fibers to form narrow and short IESs [Fig. 1(a)–1(c)]. The physiological dimensions of splenic IESs are 0.25–1.2 μm in height

TABLE II. The computed viscoelastic parameters (including shear modulus μ and membrane viscosity η_m) of the age-associated RBCs with enhanced connectivity in spectrin network (n); adapted from Ref. [45].

n (%)	μ ($\mu\text{N/m}$)	η_m ($\mu\text{N/ms}$)	γ^C	γ^T
0.00	10.3	0.46	45.5	136.5
6.25	11.6	0.58	57.4	172.2
12.50	13.7	0.74	73.2	219.6
18.75	14.4	0.94	93.0	279.0
25.00	16.3	1.32	130.6	391.8

TABLE III. Geometry parameters of different sizes of splenic IESs. The symbol IES-I, having an upper limit on experimental measurement of the splenic IES [3,67], represents a wider IES. The symbol IES-II is taken a size closer to the average of the experimental measurement, representing a narrower splenic IES.

	W_s (μm)	H_s (μm)	D_s (μm)	L_s (μm)
IES-I	4.0	1.2	2.47	1.89
IES-II	3.0	0.6	1.51	2.2

(H_s), 0.9–3.2 μm in length L_s , and 2.0–4.0 μm in width W_s [3,67]. The IES dimensions reported in a recent microfluidic experiment are $H_s = 0.85 \mu\text{m}$, $L_s = 3.0 \mu\text{m}$, and $W_s = 5.0 \mu\text{m}$ [20]. Some investigators have suggested that nascent IESs may have smaller openings [68–70]; however, to the best of our knowledge, how an individual IES changes with age is still unclear. Since our primary focus was on the effects of age-related RBC morphological changes on their flow dynamics and mechanical retention in the splenic IES, we do not specifically investigate the potential effects of aging on the IES dimensions themselves. In this study, we construct two splenic IES models, as shown in Table III. Here, we consider the size of the IES-I as the upper limit of the IES, while the IES-II is in the middle range of the IES. Specifically, we choose the dimensions of the IES-I to be $H_s = 1.2 \mu\text{m}$, $L_s = 1.89 \mu\text{m}$, and $W_s = 4.0 \mu\text{m}$, and the dimensions of the IES-II to be $H_s = 0.6 \mu\text{m}$, $L_s = 2.2 \mu\text{m}$, and $W_s = 3.0 \mu\text{m}$. The IES dimensions chosen for our simulations compare well with those reported in previous *in vivo* and *in vitro* studies [3,18,20,67]. Following previous computational studies [37,43], we define the diameter of the circle, whose area is equal to that of the cross-section of the IES, as its characteristic diameter ($D_s = 2\sqrt{H_s W_s / \pi}$) to facilitate theoretical analysis. The slit openings in the IES are dynamic in nature and undergo cyclic opening and closing. According to the observations of MacDonald *et al.* [11] and Groom *et al.* [71], the opening period of the slit aperture is ≈ 10 s, while it takes about two orders of magnitude less time for a single RBC to cross the slit. Given this significant difference in timescales, the dynamic nature of the slit opening has a minimal effect on individual RBCs as they traverse the IES. In addition, the effective stiffness of RBCs is approximately 100 times less than that of endothelial cells [72]. Because of this difference in stiffness, the RBCs are more likely to deform in response to the forces exerted by the IES, while the IES remains relatively unaffected. Hence, the endothelial cells and annular stress fibers are established to be rigid cylindrical walls [Fig. 1(d)].

By far, it is still challenging to obtain quantitative data on the flow dynamics of RBCs in the human spleen. As observed and estimated by MacDonald *et al.* [11,12], the blood hematocrit (HCT) in the spleen is $\approx 64.5\%$, and the mean flow velocity is approximately 76 $\mu\text{m}/\text{s}$. Furthermore, previous *ex vivo* spleen perfusion experiments have shown that most RBCs can pass through the splenic IES under a pressure gradient of $\approx 1.0 \text{ Pa}/\mu\text{m}$ [13,14]. Therefore, we assume that the human spleen under physiological conditions is similar to the situation described above. We set the viscosity of the extracellular fluid to 7.0 cP, which is calculated using the empirical relationship $\ln(\eta_b) = \ln(\eta_p) + k\text{HCT}$, where η_b is the viscosity of whole blood, η_p is the viscosity of blood plasma (1.2 cP), and k is an empirical factor (0.025) [73]. We also apply a pressure gradient of 1.0 $\text{Pa}/\mu\text{m}$, which yields an average fluid velocity of $\approx 100 \mu\text{m}/\text{s}$. These parameters are in the same order of magnitude as those used in previous experimental [18,67] and simulation studies [37,41], ensuring that our model is consistent with existing knowledge and providing a solid basis for our results.

In all simulations, the RBC is initially placed on the left side of the splenic IES at a distance of 10 μm from the entrance of the splenic IES. The orientation of how the RBC passes through the splenic IES affects its dynamics. In this work, we consider three different orientation conditions, where the initial orientation of the RBC is depicted by the roll angle θ_0 and the pitch angle ϕ_0 , see

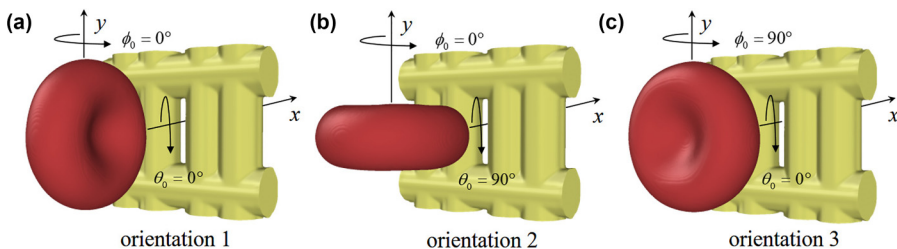


FIG. 2. Definition of the initial cell orientations. The line between the centroid of the RBC and IES is consistent with the flow direction (along the x axis). Orientations 1–3 indicate that the direction of the RBC thickness is consistent with the slit height direction, width direction, and flow direction, respectively.

Fig. 2. For simplicity, the line between the centroid of the RBC and the splenic IES is in the same direction as the pressure gradient. And the orientation is not restricted while flowing.

The DPD parameters between the fluid particles are set so that the fluid particles have a stable particle density, and the fluid viscosity can be mapped to ≈ 7.0 cP for extracellular fluid and ≈ 6.0 cP for cytosol. The DPD parameters between the fluid and solid particles are set and tested as no-slip boundary conditions. The fluids inside and outside the cell do not interact. In addition, only weak repulsive forces of $a_{ij} = 1.0$ exist between particles that are not connected by springs on the RBC membrane to ensure stable mechanical properties of the RBC model. The parameters are listed in Table S1. The simulation system is placed in a simulation box of $27 \mu\text{m} \times 13 \mu\text{m} \times 11 \mu\text{m}$. Periodic boundary conditions are applied in all x , y , and z directions. All DPD simulations are performed using a modified version of LAMMPS [74], and the time integration of the motion equations is computed through a modified velocity Verlet algorithm with a time step of $\Delta t = 5 \times 10^{-4} \tau \approx 0.432 \mu\text{s}$, which balances the normal operation and computational efficiency of the RBC model. A typical simulation in our study computes $1.0\text{--}5.0 \times 10^6$ steps, corresponding to approximately $0.432\text{--}2.16$ s. This simulation duration allows us to capture the entire RBC crossing process, which takes about $0.1\text{--}0.4$ s.

III. RESULTS AND DISCUSSION

In this section, we employ the DPD-based mesoscopic RBC model to explore the mechanism of splenic retention of age-associated RBCs, focusing on the effects of cell viscoelastic properties, RBC size, and IES size on the flow dynamics of senescent RBC passage through the splenic IESs.

A. Effects of viscoelastic properties of age-associated red blood cells on their flow dynamics in splenic interendothelial slits

We first apply the IES-I and RBC-I to study the effects of the cell viscoelastic parameters on the flow dynamics of the age-associated RBCs when passing through the splenic IES. Figures 3(a)–3(c) show the evolution of centroid displacement of the RBC (x_c) with time (t), x -axis length of the RBC (L_x) with x_c , and transit time (t_R) with respect to n for the RBC with three different initial orientation conditions, respectively. In each simulation case, the RBC undergoes a deceleration process upon entering the IES, a deceleration process within the IES, and an acceleration process upon exiting the slit in all cases. Still, it is subject to different shape deformations and dynamic motions under different initial orientations.

In the case of orientation 1 [$\theta_0 = \phi_0 = 0^\circ$, Fig. 2(a)], the RBC presents a simple dynamic motion process, elongating as entering the IES and recovering due to elasticity after leaving the IES. As n increases, the deformation mode remains almost unchanged, but the deformation gets smaller and slower [black dashed line in Fig. 3(b)]. For this case, the L_x values change smoothly as the RBC passage through the IES, which means it enters the IES easily. In the case of orientation 2

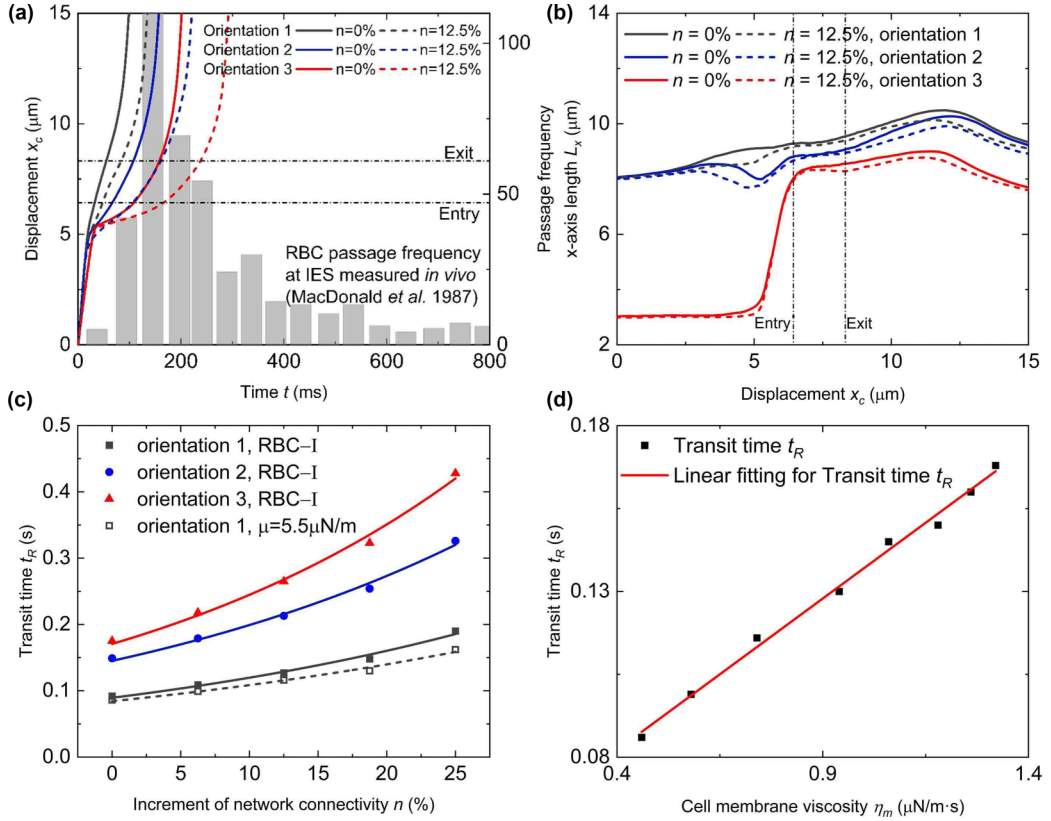


FIG. 3. (a) Displacement of cell centroid, (b) cell elongation length along flow direction, and (c), (d) transit time for RBC-I with different viscoelastic parameters during its passage through IES-I. For comparison, the frequency distribution of RBC passage through IESs measured *in vivo* [11] is depicted in panel (a), corresponding to the right axis.

$[\theta_0 = 90^\circ, \phi_0 = 0^\circ]$, Fig. 2(b)], the centroid of the RBC moves more slowly than that for the case of orientation 1 when crossing the IES [blue lines in Fig. 3(a)], and the value of L_x has a sudden decline [the two blue lines in Fig. 3(b)], which means that the RBC gets shorter due to impact into the IES. In the case of orientation 3 $[\theta_0 = 0^\circ, \phi_0 = 90^\circ]$, Fig. 2(c)], the RBC in the direction of thickness is stretched out when it enters the IES, manifested by a dramatic increase in L_x value [the two red lines in Fig. 3(b)].

In the case of orientation 1, the transit time of the RBC with $n = 0\%$ is around 0.092 s, which is close to the mode of the transit time, $t_R \approx 0.1$ s, measured in the rat spleen by MacDonald *et al.* [11]. A previous simulation study under a similar computational condition shows that the computed t_R value is about 0.028 s [39], much lower than the values obtained in previous experimental measurements [11] and our computational results. One possible reason is that their studies underestimated the membrane viscosity of the RBC. In addition, as n increases, the transit time grows exponentially for all test orientation cases [Fig. 3(c)]. This trend is similar to our previous observation on the functional dependence of cell membrane viscosity with respect to n [45]. For example, the transit time increases exponentially from 0.092 to 0.19 s with n increases from 0% to 25% for the case of orientation 1. It increases from 0.149 to 0.326 s and from 0.175 to 0.428 s for the cases of orientations 2 and 3, respectively [Fig. 3(c)]. The longest transit time occurs for the case of orientation 3, and the shortest one is for the case of orientation 1, which is consistent with previous computational results [36,39].

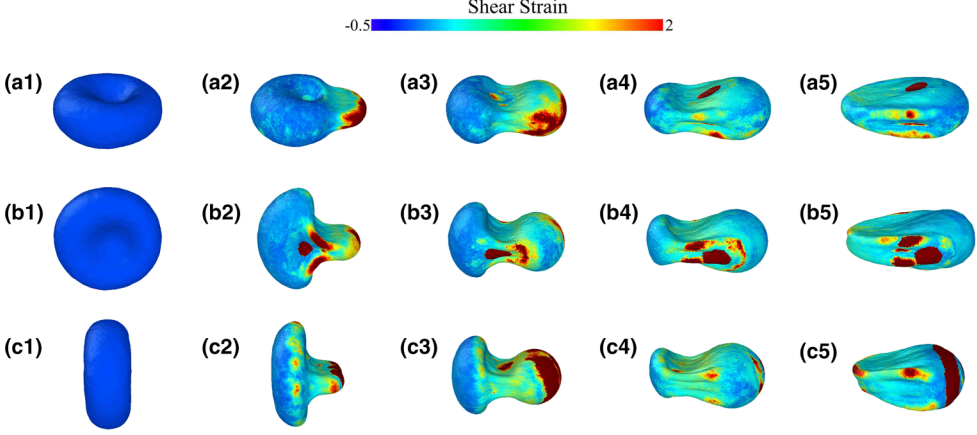


FIG. 4. Shear strain contours of RBC-I with $n = 0\%$ when passing through the IES-I with different initial orientations. Panels (a1)–(a5), (b1)–(b5), and (c1)–(c5) represent orientation 1, 2, and 3, respectively.

Next, we use the RBC-I with different viscous membrane properties at a fixed shear modulus ($\mu = 5.5 \mu\text{N}/\text{m}$) to probe the effect of membrane viscosity on the RBC transit time. It is known that the RBCs do rotate and twist in most previous experimental studies. In a previous computational study, Salehyar *et al.* showed that the RBC would rotate or twist if the centroid of the RBC deviated from the axis of symmetry of the splenic slit [39]. They found that the mechanical behavior of the RBC starting from the simulation cases of orientation 2 (when the initial orientation angle is slightly off from 90°) and orientation 3 (when the centroid of the cell is not aligned with the slit in the direction of flow) often switches to a scenario similar to orientation 1, by which they thought that the RBC with orientation 1 might be the most common mode of translocation under physiological conditions. Following this computational study, we consider the RBC simulations only for the case of orientation 1. Figure 3(d) shows the functional dependence of cell transit time with respect to cell membrane viscosity. The value of t_R changes from 0.086 to 0.162 s, which increases linearly with η_m , and the best-fit regression is $t_R = 0.091\eta_m + 0.046$ with $R^2 = 0.99$.

To further quantify the deformation of the RBCs when passing through the splenic IESs, we compute the local shear strain (γ_s) of the RBCs during their passage, given by

$$\gamma_s = \sqrt{E_{xy}^2 + E_{yz}^2 + E_{zx}^2 + \frac{1}{6}[(E_{xx} - E_{yy})^2 + (E_{xx} - E_{zz})^2 + (E_{zz} - E_{yy})^2]}, \quad (18)$$

where E_{mn} ($m, n = x, y, z$) is the component of Green-Lagrangian strain tensor $\mathbf{E} = (\mathbf{F}^T \mathbf{F} - \mathbf{I})/2$, and $\mathbf{F} = \partial \mathbf{x} / \partial \mathbf{X} = \mathbf{I} + \partial \mathbf{u} / \partial \mathbf{X}$ is the deformation gradient tensor, where \mathbf{x} , \mathbf{X} , \mathbf{u} , \mathbf{I} are the current coordinates, the initial coordinates, the displacement vectors of the particles, and the identity matrix, respectively. Figures 4(a1)–4(a5) displays the morphological changes and distributions of the membrane shear strain of the RBC-I with $n = 0\%$ for the case of orientation 1. It shows that the cell deformation occurs first in the downstream part of the RBC membrane. When the RBC is in the middle part of the IES, its surface area inside the IES folds slightly inward. Eventually, the RBC is pulled out of the long tail and leaves the IES, which is consistent with previous *in vivo* observations by MacDonald *et al.* [11,12]. In the case of orientation 2, as shown in Fig. 4(b2), the RBC hits the IES first, which induces a reduction in cell elongation length. The maximum γ_s occurs in the concave of the RBC and is accompanied by folding during the entire transit process; see Figs. 4(b3)–4(b5). In the case of orientation 3, the inflection point occurs later than the other two cases, accompanied by a surge in L_x value. As the RBC enters the IES, its downstream concave is rapidly pulled out [Fig. 4(c2)]. The RBC is then elongated in the direction of cell thickness but is slightly shorter than those in the former two cases. As shown in Figs. 4(c3)–4(c5), the maximum

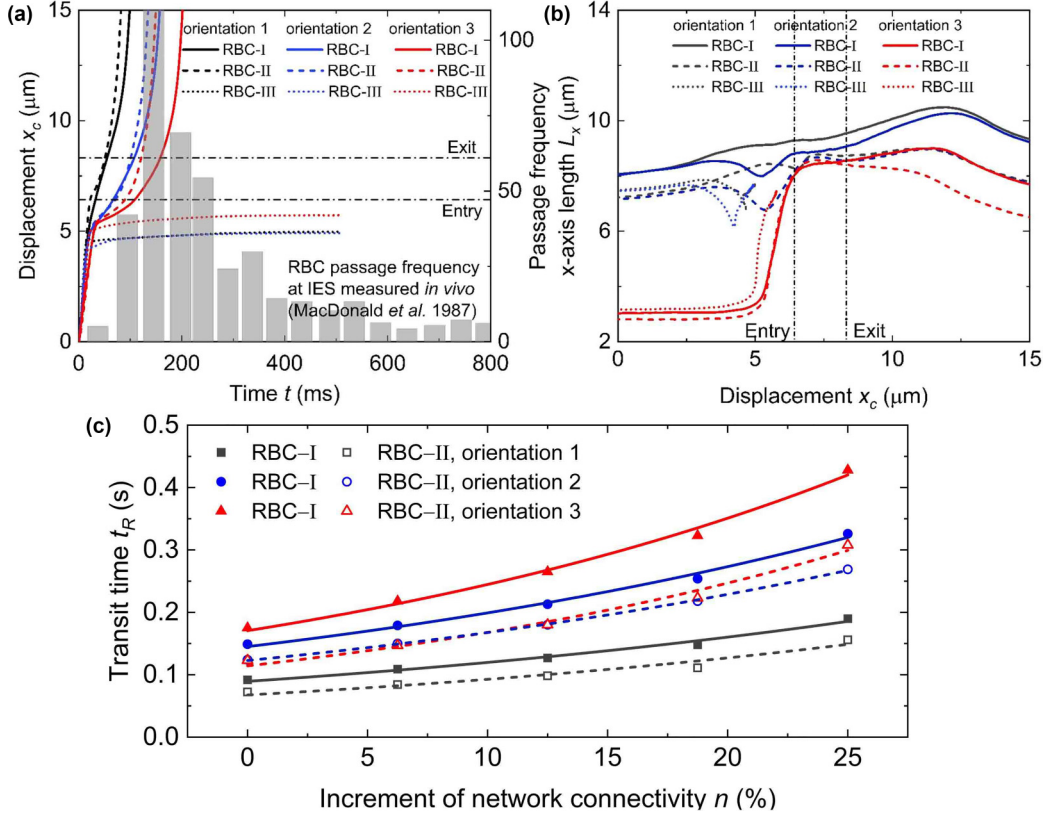


FIG. 5. (a) Displacement of cell centroid, (b) cell elongation length along flow direction, and (c) transit time for RBCs of different sizes during their passage through IES-I. For comparison, the frequency distribution of RBC passage through IESs measured *in vivo* [11] is depicted in panel (a), corresponding to the right axis.

γ_s occurs in the concave, similar to the case of orientation 2, but large deformations occur in more areas. While leaving from the IES, the bulged head of the RBC is more extensive, and the tail folds more noticeably.

Among all the test cases, the RBCs for the cases of orientation 3 take the longest transit time to pass through the IES. Such results illustrate that more significant and complex deformations of RBCs prolong their transit time through the splenic IESs and that the membrane viscosity of RBCs significantly affects the transit time.

B. Cell size alterations in age-associated red blood cells on their flow dynamics in splenic interendothelial slits

We perform three parallel DPD simulations with different RBCs (i.e., RBC-I, RBC-II, and RBC-III) to investigate the effect of altered cell size on the traversal dynamics of the age-associated RBCs through the splenic IESs. In Figs. 5(a)–5(c), we compare the x_c-t , L_x-x_c , and t_R-n curves between the RBC simulation results. First, the RBC-II has a similar deformation pattern to the RBC-I under all three different initial orientation conditions. However, it deforms smaller and takes a shorter time to pass through the splenic IES. Compared with the simulation cases of RBC-I, the RBC-II for orientation 1 is significantly different in two ways. On the one hand, as shown in Fig. 5(a), the speed inflection point appears later because of its smaller size. The centroid of the RBC is thus closer to the slit entrance when the RBC collides with the IES. On the other hand, as shown in Fig. 5(b),

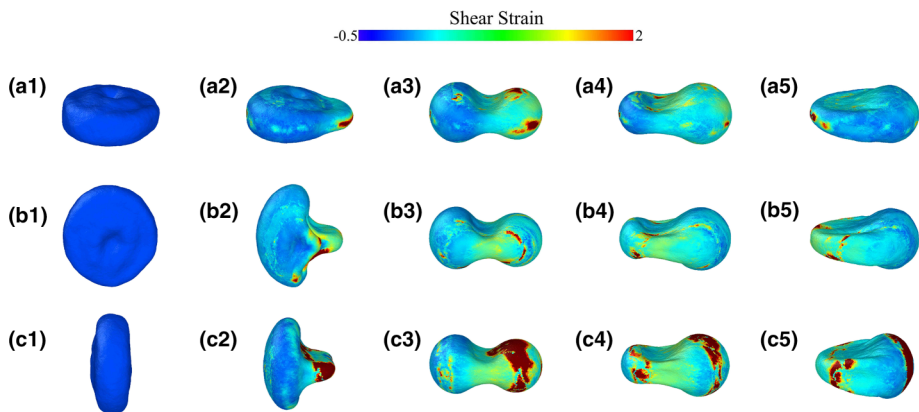


FIG. 6. Shear strain contours of RBC-II with $n = 0\%$ when passing through the IES-I with different initial orientations. Panels (a1)–(a5), (b1)–(b5), and (c1)–(c5) represent orientations 1, 2, and 3, respectively.

there is a noticeable drop in L_x after the RBC enters the IES. It is because when the RBC-II is in the middle part of the IES, causing a reduction in its elongation length, as shown in Fig. 6(a3). Second, the RBC-III is trapped by the IES under all three initial orientation conditions, indicating that the reduced S_A/V is still a key factor in their mechanical retention for senescent RBCs whose volume decrease. Typically, in the cases of orientations 1 [Figs. 7(a1)–7(b4)] and 2 [Figs. 7(b1)–7(b4)], the value of L_x of the RBC-III is first reduced due to collision and compression [Figs. 7(a2) and 7(b2)] and then increases because of being struggled to get into the IES [Figs. 7(a3) and 7(b3)].

The values of cell transit time are, respectively, 0.073–0.156 s, 0.124–0.269 s, and 0.123–0.308 s for the RBC-II simulation cases with orientations 1, 2, and 3, see Fig. 5(c). These values are significantly reduced compared with the simulation cases with the RBC-I. Figure 6 performs the shape deformation and distribution of the membrane shear strain of the RBC-II with $n = 0\%$ when passing through the IES-I. Compared with the RBC-I simulation results, the RBC-II deformation pattern is similar. These smaller RBCs also become gourd shaped as they enter the IES. Furthermore, when leaving the IES, they get closer to the dumbbell-shaped than the RBC-I and have a bulged head

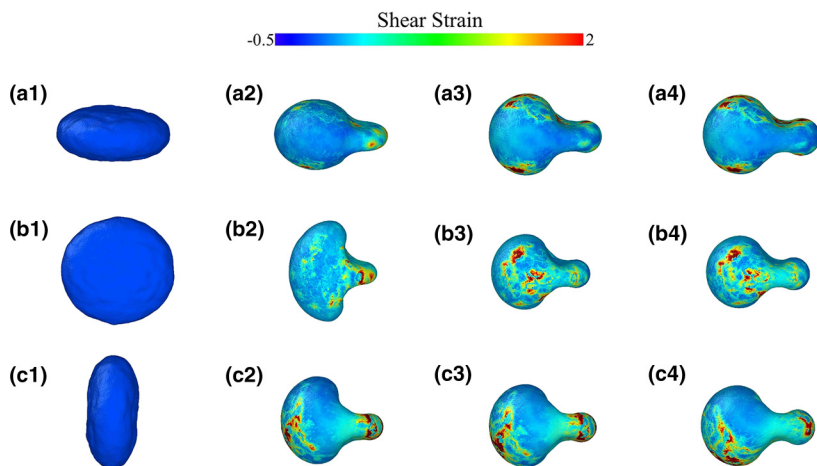


FIG. 7. Shear strain contours of RBC-III with $n = 0\%$ when trapped by the IES-I with different initial orientations. Panels (a1)–(a4), (b1)–(b4), and (c1)–(c4) represent orientations 1, 2, and 3, respectively.

TABLE IV. The viscoelastic parameters used for RBCs at different SI.

SI	n (%)	μ ($\mu\text{N}/\text{m}$)	η_m ($\mu\text{N}/\text{ms}$)
0.688	0.00	10.3	0.46
0.753	12.50	13.7	0.74
0.764	18.75	14.4	0.94
0.817	25.00	16.3	1.32

and elongated tail. Nevertheless, some details in cell shape deformation become different, such as less buckling and less deformation. Specifically, no buckling appears at the bridge, and no large deformation occurs when the RBC is in the middle of the IES for the case of orientation 1. There is no considerable strain when leaving the IES. In the case of orientation 2, the RBC also infolds when entering the IES, yet the deformation here is much less than that of the RBC-I. Besides, the comparison between Figs. 4(a4)–4(c4) and Fig. 6(a4)–6(c4) shows that the tail of the RBC-II does not adhere to the IES wall when leaving the IES, which is different from that of RBC-I. Generally, the RBC-II is smaller and shorter in diameter, causing a shorter journey, less resistance, and less deformation as it traverses the IES. Such alterations make it easier for the RBC-II to pass through the IES instead of being trapped due to an enlarged S_v . Even becoming smaller, the age-associated RBC (RBC-II) with greater membrane viscosity requires a longer transit time to pass through the splenic IES than a young healthy one (RBC-I). Such an extended transit period may increase the probability of macrophage recognition of these senescent RBCs.

C. Coupling effect of cell size and viscoelasticity of age-associated red blood cells on their flow dynamics in splenic interendothelial slits

The results in the previous sections show that both the cell size and viscoelastic properties can affect the flow dynamics of old RBCs in splenic IESs. To further explore the coupling effect of these two factors, we perform and compare two different sets of simulations with the same settings except for the cell viscoelastic parameters. One set of simulations where cell size is varied but mechanical parameters are fixed ($n = 0\%$), and another set of simulations where both cell size and mechanical parameters are varied; see Table IV for details. Note that the viscoelastic parameters change only for cells that can pass through the IESs. For each group, the SI values are derived from the measured data in the microfluidic experiment of Garcia-Herreros *et al.* [20]. For each SI, three representative RBCs are simulated, whose volume values are close to the average in Ref. [20]. For example, $V = 95.6 \mu\text{m}^3$, $97.6 \mu\text{m}^3$, $99.5 \mu\text{m}^3$ (mean $\pm 2\%$) is used for SI = 0.688. For brevity, the initial orientation is set to orientation 1, and other conditions are set as in the previous sections.

In Fig. 8, we plot the simulation results of the two groups described above and compare them with the available experimental data [20]. The simulation results show that the RBCs with SI $\gtrsim 0.87$ cannot pass through the IES, while it is SI $\gtrsim 0.90$ for the experimental results by Garcia-Herreros *et al.* [20]. For the cells that can pass through the IESs, the t_R decreases with SI (slope = -0.26) when the viscoelastic properties of the RBCs are kept constant. At the same time, it shows an increasing tendency with SI (slope = 0.46) for the group with altered viscoelastic properties of the cells. The former phenomenon contradicts the trend reported by Garcia-Herreros *et al.* [20], while the latter shows the same trend. These comparisons confirm the previously mentioned results that the reduced size of senescent RBCs would allow them to pass through the IESs in less time, despite being spherical. At the same time, the increased shear modulus and membrane viscosity during cell aging would slow down this process. Such results indicate that in extreme cases of the aging process, the high sphericity of these RBCs is the key factor in being trapped by the IESs. On the other hand, in earlier stages of the aging process, the increasing shear modulus and membrane viscosity may play an essential role in impeding the passage.

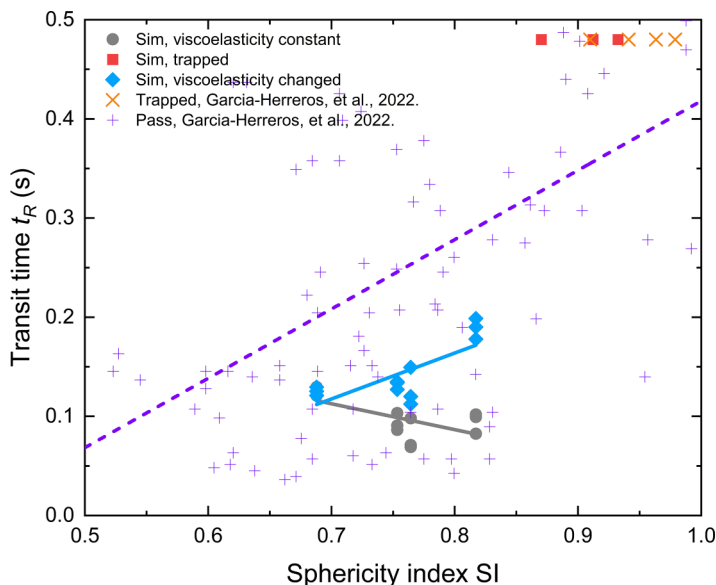


FIG. 8. Dependence of cell transit time on sphericity index (SI) of the RBC. Each point represents the transit time for a single RBC. Cell volume and surface area values are derived from *in vitro* microfluidic experiment [20], whose results are also compared. Blue and gray solid lines are fit from simulations, and the purple dashed line is reproduced from Ref. [20].

To the best of our knowledge, no experimental studies have reported the simultaneous changes in cell size and viscoelastic properties during cell aging or mechanical fatigue process; therefore, this is still a tentative study with an artificial combination of different research results. Future studies can investigate this more systematically when such data are obtained from companion microfluidic experiments.

D. Effects of interendothelial slit size and pressure gradient on the mechanical retention of age-associated red blood cells

In this section, we apply a narrower slit (IES-II) and a more significant pressure gradient of $5.0 \text{ Pa}/\mu\text{m}$ to investigate the mechanical retention of age-associated RBCs further. For simplicity, the shear modulus and membrane viscosity of the RBCs are set to be the same as those used with $n = 0\%$, and only the case of orientation 1 is considered. It is worth noting that the membrane viscosity and initial orientation of the RBCs do not affect their ability to pass through the splenic IESs.

Figure 9 shows the dynamic motion and shape deformation of RBCs under two different pressure gradients (i.e., 1.0 and $5.0 \text{ Pa}/\mu\text{m}$). At a lower pressure gradient ($1.0 \text{ Pa}/\mu\text{m}$), the RBC-I passes through the narrow IES after experiencing a significant and slow deformation, while the RBC-II and RBC-III fail to pass. For the RBC-I, it reaches the dumbbell shape after experiencing a more significant deformation, and its tail is pulled longer when escaping the IES [Figs. 10(a1)–10(a5)]. However, the other cells fail in the transition from gourd to dumbbell-shaped, as shown in Figs. 10(b1)–10(b4) and 10(c1)–10(c4). Furthermore, at a higher pressure gradient of $5.0 \text{ Pa}/\mu\text{m}$, the RBC-II can deform more to pass through the splenic IES quickly [Figs. 10(b1)–10(b4)], while the RBC-III is still trapped [Figs. 10(c1)–10(c4)]. The blue dashed lines in Fig. 9 and Fig. 11(b1)–10(b5) demonstrate that the RBC-II deforms faster when entering the narrow IES-II, and its elongation decreases instantaneously when the RBC moves forward from the dumbbell state. Comparing Figs. 10 and 11, all cells are sheared more strongly under a more significant pressure gradient, damaging RBCs.

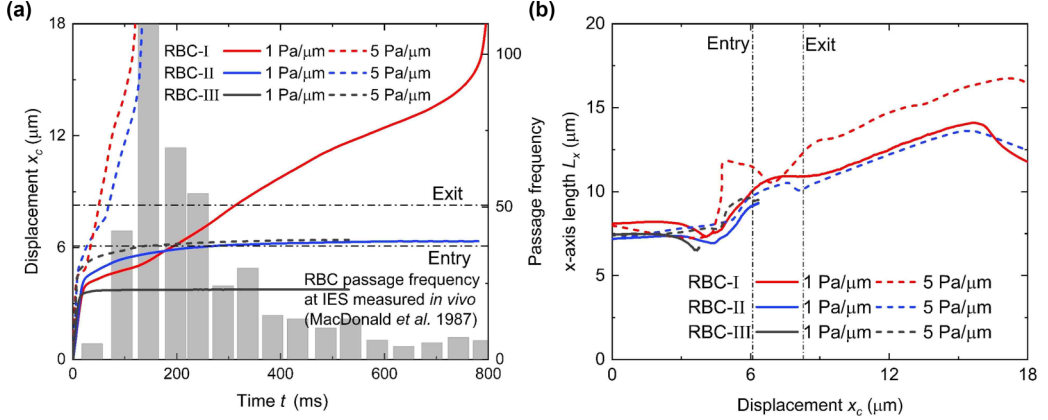


FIG. 9. (a) Displacement of cell centroid and (b) cell elongation along flow direction for RBC-I, RBC-II, and RBC-III with $n = 0\%$ during their passage through the IES-II under different pressure gradient levels. For comparison, the frequency distribution of RBC passage through IESs measured *in vivo* [11] is depicted in panel (a), corresponding to the right axis.

To further investigate the effect of IES size on mechanical retention of RBCs with different surface areas and volumes. Several cases with different S_A and V are performed under the pressure gradient of $1.0 \text{ Pa}/\mu\text{m}$; see scatters in Fig. 12(a). Moreover, following the theoretical model proposed by Pivkin *et al.* [37], we consider the critically deformed RBC as a dumbbell-shaped cell when passing through a specific rigid IES as shown in Fig. 12(a). The dumbbell shape can be considered a combination of two spheres and a torus. The cross-section of the splenic IES in the y - z plane is assumed to be circular with a diameter of D_s . In the critical case, the surface area and volume of the RBC are computed by

$$S_A = 4(2\pi R^2 - \pi R h) + 2\pi L_s \alpha \left(\frac{D_s}{2} + \frac{L_s}{2} - \frac{L_s \sin \alpha}{2\alpha} \right), \quad (19)$$

$$V = 2 \left[\frac{4}{3} \pi R^3 - \frac{1}{3} \pi h^2 (3R - h) \right] + \frac{\pi L_s}{2} (R + L_s) \cos \alpha (R \sin 2\alpha - L_s \alpha) + \frac{\pi}{4} \left(L_s^3 \sin \alpha - \frac{L_s^3 \sin^3 \alpha}{3} \right), \quad (20)$$

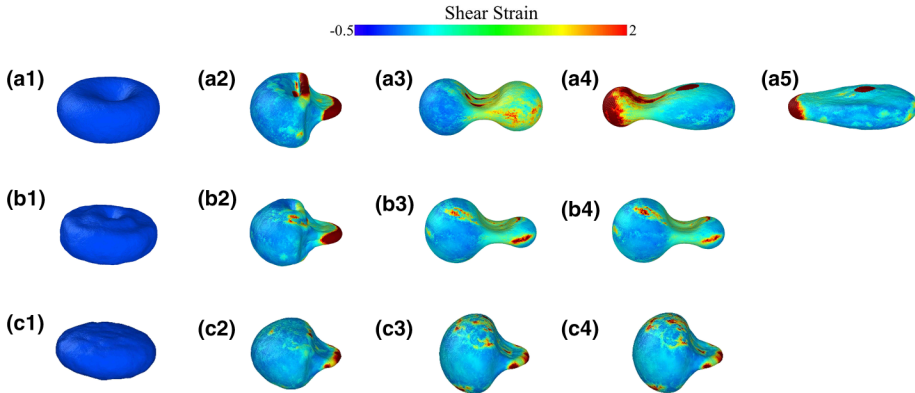


FIG. 10. Shear strain contours of RBC-I (a1)–(a5), RBC-II (b1)–(b4), and RBC-III (c1)–(c4) with $n = 0\%$ when passing through or being trapped in the IES-II under pressure gradient of $1.0 \text{ Pa}/\mu\text{m}$.

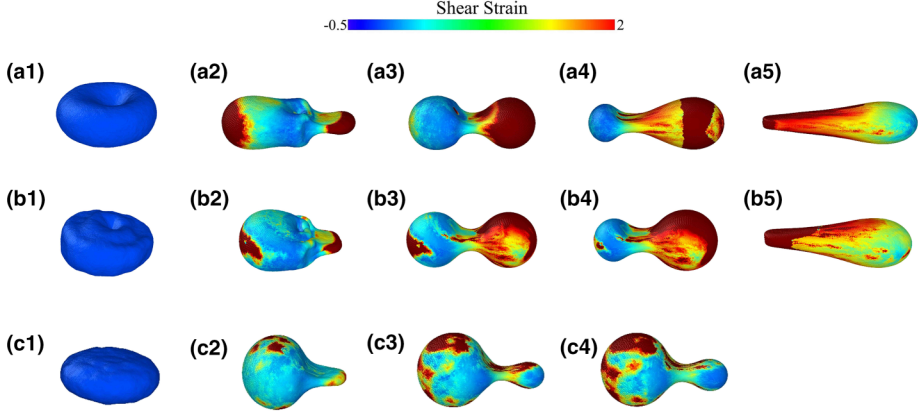


FIG. 11. Shear strain contours of RBC-I (a1)–(a5), RBC-II (b1)–(b5), and RBC-III (c1)–(c4) with $n = 0\%$ when passing through or being trapped in the IES-II under pressure gradient of $5.0 \text{ Pa}/\mu\text{m}$.

where h is the height of the spherical cap cut by the y - z plane at the point of contact p , and α is an angle of the torus part as shown in Fig. 12(a), given by

$$h = R - R \sqrt{1 - \frac{\left(\frac{D_s}{2} + \frac{L_s}{2}\right)^2}{\left(R + \frac{L_s}{2}\right)^2}}, \quad (21)$$

$$\alpha = \arccos \left[\frac{\left(\frac{D_s}{2} + \frac{L_s}{2}\right)}{\left(R + \frac{L_s}{2}\right)} \right]. \quad (22)$$

We then rewrite Eq. (20) as $V = f(R)$, and its inverse function can be written as $R = f^{-1}(V)$. Thus, Eqs. (21) and (22) can be expressed as $h = h(R) = h(f^{-1}(V)) = g_1(V)$ and $\alpha = \alpha(R) = \alpha(f^{-1}(V)) = g_2(V)$, respectively. With the substitution of Eqs. (20)–(22) into Eq. (19), one can

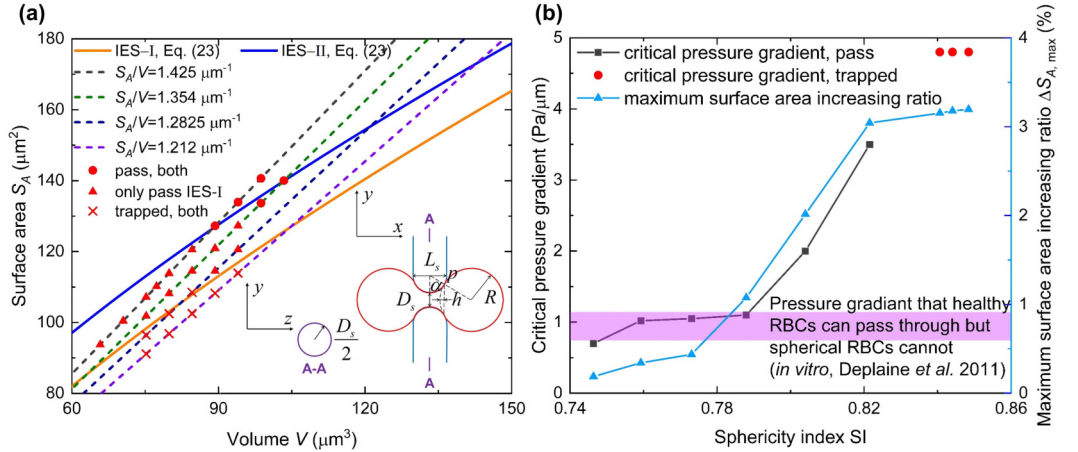


FIG. 12. (a) Analytical prediction and numerical results (under pressure gradient of $1.0 \text{ Pa}/\mu\text{m}$) of splenic IES retention for RBCs. (b) Critical pressure gradient and maximum surface area increasing ratio of RBCs under the critical pressure gradient conditions ($S_A/V = 1.425 \mu\text{m}^{-1}$, and IES-II). The red circle points, considered trapped RBCs, represent those that cannot pass through the IES under the pressure gradient up to $10.0 \text{ Pa}/\mu\text{m}$. *In vitro* experimental results [67] are depicted for comparison.

obtain the critical relationship between the RBC surface area and volume given by

$$S_A = 4\{2\pi[f^{-1}(V)]^2 - \pi f^{-1}(V)g_1(V)\} + 2\pi L_s g_2(V) \left\{ \frac{D_s}{2} + \frac{L_s}{2} - \frac{L_s \sin[g_2(V)]}{2g_2(V)} \right\}. \quad (23)$$

The orange and blue solid lines in Fig. 12(a) indicate the S_A - V function of RBCs allowed to pass through IES-I and IES-II, respectively. The space above the lines is predicted to be able to pass through the slit it represents. The red square, triangle, and cross points represent the RBCs that can pass through the IESs, which can only pass through IES-I, and RBCs trapped by two IESs, respectively. The results show that most simulation results agree with the analytical prediction. For each S_A/V (dashed lines), these curves are steeper than the solid lines. This shows that when the aging and smaller RBCs are more likely to be trapped by the slit if the S_A/V remains unchanged, the smaller S_A/V can facilitate this process.

Using $S_A/V = 1.425 \mu\text{m}^{-1}$, IES-II as an example, we investigate the critical pressure gradient of RBC-I at shrinkage of 95% to 68%, corresponding SI of 0.759 to 0.848. As shown in Fig. 12(b), the critical pressure gradient is $\approx 0.7 \text{ Pa}/\mu\text{m}$ for RBC-I, and it creeps up to $\approx 1.1 \text{ Pa}/\mu\text{m}$ for the RBC with SI = 0.788, which agrees with the range measured in *in vitro* devices that healthy RBCs can pass through while spherical RBCs cannot [67]. As the SI increases to 0.822, the critical pressure gradient rapidly increases to $\approx 3.5 \text{ Pa}/\mu\text{m}$. Moreover, as the SI increases to greater than 0.841, the RBCs lose the ability to pass through the narrow slit. The RBCs undergo extreme restriction during the passage, slightly increasing their surface area. We monitor the increase of cell surface area (ΔS_A) under the critical pressure gradient, and the maximum values ($\Delta S_{A,\text{max}}$) are shown in Fig. 12(b). As the cell size shrinks to 90% (SI = 0.773), the $\Delta S_{A,\text{max}}$ slowly increases to no more than 0.44%. Furthermore, when the cell size shrinks further down to 75% (SI = 0.822), $\Delta S_{A,\text{max}}$ increases rapidly to $\approx 3.04\%$, which reaches the threshold for RBC lysis, $\Delta S_A = 24\%$ [75]. These RBCs are considered to have the potential to pass through the narrow IES under a high-pressure gradient, such as RBC-II mentioned earlier in this section. However, significant shear and area stress will cause great damage to these cells and promote aging. As the RBC shrinks to 68% (SI increases to 0.848), $\Delta S_{A,\text{max}}$ slowly increases to $\approx 3.20\%$ under $10.0 \text{ Pa}/\mu\text{m}$. However, the increased S_A of these RBCs is much smaller than the one that IES-II allows to pass, which causes them to remain trapped under the high-pressure gradient. Such a situation may prolong the high deformation of these extremely senescent RBCs, making them more likely to rupture or lyse [75] and enhancing their clearance by macrophages than intact ones [76].

IV. CONCLUSION

In this study, we employ a DPD-based mesoscopic RBC model to investigate the flow dynamics and mechanical retention of age-associated RBCs when crossing the splenic IESs. We show that an enhanced membrane viscosity of the age-associated RBCs significantly slows down the cell passage process, and the posture of the circulating RBCs also plays an essential role in their traversal dynamics through the splenic IESs. Furthermore, before getting extremely spherical to be trapped, the age-associated RBCs with reduced volume differ in deformation mode from the normal young ones with fewer buckling and minor deformation, which shortens the transit time. Additionally, narrower IESs make it harder for RBCs to get through. Only if one increases the pressure gradient to let the RBCs deform more can they get a chance to pass, which also brings more significant damage and promotes the aging process. In the case of extreme aging, the increase in surface area by more than 3% still cannot make it pass through some narrow slits, which significantly increases the probability of its lysis. This view is also supported by the fact that RBCs with high fatigue levels are more likely to lyse [20].

It is generally believed that the altered cell shape, poor deformability, and diminutive S_A/V ratio are crucial factors that cause RBC entrapment in the spleen. However, the splenic IES clearance process is blurred by the reduced cell size of the age-associated RBCs. In this study, our computational

results reveal some possible reasons for the mechanical retention of the age-associated RBCs by the splenic IESs. It shows that extreme SI still plays an essential role in retaining senescent RBCs. However, at some stages in the aging process, the reduced cell size does not extend the transit time, while the increased viscoelasticity does. Such derivation might be attributed to the combined data sets chosen from two separate experiments [20,24] since there is no systematic report on the alterations in cell size and viscoelastic properties simultaneously during cell aging. The systematic computational investigation of the coupling effects on RBC passage through the splenic IESs requires more guidance from companion microfluidic experiments.

ACKNOWLEDGMENTS

This work was supported by the National Key R&D Program of China (Grant No. 2022YFA1203202), the National Natural Science Foundation of China (Grants No. 12072318 and No. 11832017), and the Zhejiang Provincial Natural Science Foundation (Grant No. LY22A020004). Simulations were performed at the Beijing Super Cloud Computing Center (BLSC).

-
- [1] R. E. Mebius and G. Kraal, Structure and function of the spleen, *Nat. Rev. Immunol.* **5**, 606 (2005).
 - [2] A. Petroianu, *The Spleen* (Bentham Science Publishers, Hilversum, The Netherlands, 2011).
 - [3] L. Chen and L. Weiss, The role of the sinus wall in the passage of erythrocytes through the spleen, *Blood* **41**, 529 (1973).
 - [4] R. E. Waugh, M. Narla, C. W. Jackson, T. J. Mueller, T. Suzuki, and G. L. Dale, Rheologic properties of senescent erythrocytes: Loss of surface area and volume with red blood cell age, *Blood* **79**, 1351 (1992).
 - [5] F. Liu, J. Burgess, H. Mizukami, and A. Ostafin, Sample preparation and imaging of erythrocyte cytoskeleton with the atomic force microscopy, *Cell Biochem. Biophys.* **38**, 251 (2003).
 - [6] G. J. Bosman, J. M. Werre, F. L. Willekens, and V. M. Novotný, Erythrocyte ageing in vivo and in vitro: Structural aspects and implications for transfusion, *Transfus. Med.* **18**, 335 (2008).
 - [7] F. L. Willekens, J. M. Werre, Y. A. Groenen-Döpp, B. Roerdinkholder-Stoelwinder, B. De Pauw, and G. J. Bosman, Erythrocyte vesiculation: A self-protective mechanism, *Br. J. Haematol.* **141**, 549 (2008).
 - [8] M. H. Antonelou, A. G. Kriebardis, and I. S. Papassideri, Aging and death signalling in mature red cells: From basic science to transfusion practice, *Blood Transfus.* **8**, s39 (2010).
 - [9] E. Ferru, K. Giger, A. Pantaleo, E. Campanella, J. Grey, K. Ritchie, R. Vono, F. Turrini, and P. S. Low, Regulation of membrane-cytoskeletal interactions by tyrosine phosphorylation of erythrocyte band 3, *Blood* **117**, 5998 (2011).
 - [10] K. E. Badior and J. R. Casey, Molecular mechanism for the red blood cell senescence clock, *IUBMB Life* **70**, 32 (2018).
 - [11] I. MacDonald, D. Ragan, E. Schmidt, and A. Groom, Kinetics of red blood cell passage through interendothelial slits into venous sinuses in rat spleen, analyzed by in vivo microscopy, *Microvasc. Res.* **33**, 118 (1987).
 - [12] I. MacDonald, E. Schmidt, and A. Groom, The high splenic hematocrit: A rheological consequence of red cell flow through the reticular meshwork, *Microvasc. Res.* **42**, 60 (1991).
 - [13] I. Safeukui, P. Buffet, G. Deplaine, S. Perrot, V. Brousse, A. Ndour, M. Nguyen, O. Mercereau-Puijalon, P. H. David, G. Milon *et al.*, Quantitative assessment of sensing and sequestration of spherocytic erythrocytes by the human spleen, *Blood* **120**, 424 (2012).
 - [14] I. Safeukui, P. A. Buffet, G. Deplaine, S. Perrot, V. Brousse, A. Sauvanet, B. Aussilhou, S. Dokmak, A. Couvelard, D. Cazals-Hatem, O. Mercereau-Puijalon, G. Milon, P. H. David, and N. Mohandas, Sensing of red blood cells with decreased membrane deformability by the human spleen, *Blood Adv.* **2**, 2581 (2018).

- [15] D. Quinn, I. V. Pivkin, S. Y. Wong, K. Chiam, M. Dao, G. E. Karniadakis, and S. Suresh, Combined simulation and experimental study of large deformation of red blood cells in microfluidic systems, *Ann. Biomed. Eng.* **39**, 1041 (2011).
- [16] S. Sakuma, K. Kuroda, C. H. D. Tsai, W. Fukui, F. Arai, and M. Kaneko, Red blood cell fatigue evaluation based on the close-encountering point between extensibility and recoverability, *Lab Chip* **14**, 1135 (2014).
- [17] J. Picot, P. A. Ndour, S. D. Lefevre, W. El Nemer, H. Tawfik, J. Galimand, L. Da Costa, J.-A. Ribeil, M. de Montalembert, V. Brousse, B. Le Piouffe, P. Buffet, C. Le Van Kim, and O. Francais, A biomimetic microfluidic chip to study the circulation and mechanical retention of red blood cells in the spleen, *Am. J. Hematol.* **90**, 339 (2015).
- [18] P. Gambhire, S. Atwell, C. Iss, F. Bedu, I. Ozerov, C. Badens, E. Helfer, A. Viallat, and A. Charrier, High aspect ratio sub-micrometer channels using wet etching: Application to the dynamics of red blood cell transiting through biomimetic splenic slits, *Small* **13**, 1700967 (2017).
- [19] A. Namvar, A. J. Blanch, M. W. Dixon, O. M. Carmo, B. Liu, S. Tiash, O. Looker, D. Andrew, L.-J. Chan, W.-H. Tham *et al.*, Surface area-to-volume ratio, not cellular viscoelasticity, is the major determinant of red blood cell traversal through small channels, *Cell. Microbiol.* **23**, e13270 (2021).
- [20] A. Garcia-Herreros, Y.-T. Yeh, Z. Peng, and J. C. Del Alamo, Cyclic mechanical stresses alter erythrocyte membrane composition and microstructure and trigger macrophage phagocytosis, *Adv. Sci. (Weinheim, Ger.)* **9**, 2201481 (2022).
- [21] Y. Qiang, A. Sissoko, Z. L. Liu, T. Dong, F. Zheng, F. Kong, J. M. Higgins, G. E. Karniadakis, P. A. Buffet, S. Suresh, and M. Dao, Microfluidic study of retention and elimination of abnormal red blood cells by human spleen with implications for sickle cell disease, *Proc. Natl. Acad. Sci. USA* **120**, e2217607120 (2023).
- [22] Y. Qiang, J. Liu, and E. Du, Dynamic fatigue measurement of human erythrocytes using dielectrophoresis, *Acta Biomater.* **57**, 352 (2017).
- [23] R. J. Asaro, Q. Zhu, and P. Cabrales, Erythrocyte aging, protection via vesiculation: An analysis methodology via oscillatory flow, *Front. Physiol.* **9**, 1607 (2018).
- [24] Y. Qiang, J. Liu, M. Dao, S. Suresh, and E. Du, Mechanical fatigue of human red blood cells, *Proc. Natl. Acad. Sci. USA* **116**, 19828 (2019).
- [25] S. M. Hosseini and J. J. Feng, A particle-based model for the transport of erythrocytes in capillaries, *Chem. Eng. Sci.* **64**, 4488 (2009).
- [26] M. Deng, X. Li, H. Liang, B. Caswell, and G. E. Karniadakis, Simulation and modelling of slip flow over surfaces grafted with polymer brushes and glycocalyx fibres, *J. Fluid Mech.* **711**, 192 (2012).
- [27] H. Lei, D. A. Fedosov, B. Caswell, and G. E. Karniadakis, Blood flow in small tubes: Quantifying the transition to the non-continuum regime, *J. Fluid Mech.* **722**, 214 (2013).
- [28] T. Wu and J. J. Feng, Simulation of malaria-infected red blood cells in microfluidic channels: Passage and blockage, *Biomicrofluidics* **7**, 044115 (2013).
- [29] S. Mendez and M. Abkarian, In-plane elasticity controls the full dynamics of red blood cells in shear flow, *Phys. Rev. Fluids* **3**, 101101(R) (2018).
- [30] X. Zhang, W. A. Lam, and M. D. Graham, Dynamics of deformable straight and curved prolate capsules in simple shear flow, *Phys. Rev. Fluids* **4**, 043103 (2019).
- [31] A. H. Raffiee, S. Dabiri, and A. M. Ardekani, Suspension of deformable particles in newtonian and viscoelastic fluids in a microchannel, *Microfluid. Nanofluid.* **23**, 22 (2019).
- [32] Z. Zhang, W. Chien, E. Henry, D. A. Fedosov, and G. Gompper, Sharp-edged geometric obstacles in microfluidics promote deformability-based sorting of cells, *Phys. Rev. Fluids* **4**, 024201 (2019).
- [33] X. Zhang, C. Caruso, W. A. Lam, and M. D. Graham, Flow-induced segregation and dynamics of red blood cells in sickle cell disease, *Phys. Rev. Fluids* **5**, 053101 (2020).
- [34] M. Abbasi, A. Farutin, H. Ez-Zahraouy, A. Benyoussef, and C. Misbah, Erythrocyte-erythrocyte aggregation dynamics under shear flow, *Phys. Rev. Fluids* **6**, 023602 (2021).
- [35] J. B. Freund, The flow of red blood cells through a narrow spleen-like slit, *Phys. Fluids* **25**, 110807 (2013).
- [36] S. Salehyar and Q. Zhu, Deformation and internal stress in a red blood cell as it is driven through a slit by an incoming flow, *Soft Matter* **12**, 3156 (2016).

- [37] I. V. Pivkin, Z. Peng, G. E. Karniadakis, P. A. Buffet, M. Dao, and S. Suresh, Biomechanics of red blood cells in human spleen and consequences for physiology and disease, *Proc. Natl. Acad. Sci. USA* **113**, 7804 (2016).
- [38] Q. Zhu, S. Salehyar, P. Cabrales, and R. J. Asaro, Prospects for human erythrocyte skeleton-bilayer dissociation during splenic flow, *Biophys. J.* **113**, 900 (2017).
- [39] S. Salehyar and Q. Zhu, Effects of stiffness and volume on the transit time of an erythrocyte through a slit, *Biomech. Model. Mechanobiol.* **16**, 921 (2017).
- [40] H. Li, L. Lu, X. Li, P. Buffet, M. Dao, G. E. Karniadakis, and S. Suresh, Mechanics of diseased red blood cells in human spleen and consequences for hereditary blood disorders, *Proc. Natl. Acad. Sci. USA* **115**, 9574 (2018).
- [41] Z. L. Liu, H. Li, Y. Qiang, P. Buffet, M. Dao, and G. E. Karniadakis, Computational modeling of biomechanics and biorheology of heated red blood cells, *Biophys. J.* **120**, 4663 (2021).
- [42] H. Li, Z. L. Liu, L. Lu, P. Buffet, and G. E. Karniadakis, How the spleen reshapes and retains young and old red blood cells: A computational investigation, *PLoS Comput. Biol.* **17**, e1009516 (2021).
- [43] X. Qi, S. Wang, S. Ma, K. Han, and X. Li, Quantitative prediction of flow dynamics and mechanical retention of surface-altered red blood cells through a splenic slit, *Phys. Fluids* **33**, 051902 (2021).
- [44] P. Matteoli, F. Nicoud, and S. Mendez, Impact of the membrane viscosity on the tank-treading behavior of red blood cells, *Phys. Rev. Fluids* **6**, 043602 (2021).
- [45] S. Ma, S. Wang, X. Qi, K. Han, X. Jin, Z. Li, G. Hu, and X. Li, Multiscale computational framework for predicting viscoelasticity of red blood cells in aging and mechanical fatigue, *Comput. Methods Appl. Mech. Eng.* **391**, 114535 (2022).
- [46] J. E. Mancuso and W. D. Ristenpart, Stretching of red blood cells at high strain rates, *Phys. Rev. Fluids* **2**, 101101(R) (2017).
- [47] M. Arroyo and A. DeSimone, Relaxation dynamics of fluid membranes, *Phys. Rev. E* **79**, 031915 (2009).
- [48] F. Guglietta, M. Behr, L. Biferale, G. Falcucci, and M. Sbragaglia, Lattice Boltzmann simulations on the tumbling to tank-treading transition: Effects of membrane viscosity, *Philos. Trans. R. Soc. A* **379**, 20200395 (2021).
- [49] H. Noguchi and G. Gompper, Dynamics of fluid vesicles in shear flow: Effect of membrane viscosity and thermal fluctuations, *Phys. Rev. E* **72**, 011901 (2005).
- [50] H. Noguchi and G. Gompper, Swinging and Tumbling of Fluid Vesicles in Shear Flow, *Phys. Rev. Lett.* **98**, 128103 (2007).
- [51] A. Yazdani and P. Bagchi, Influence of membrane viscosity on capsule dynamics in shear flow, *J. Fluid Mech.* **718**, 569 (2013).
- [52] O. Linderkamp and H. J. Meiselman, Geometric, osmotic, and membrane mechanical properties of density-separated human red cells, *Blood* **59**, 1121 (1982).
- [53] P. B. Conham, Difference in geometry of young and old human erythrocytes explained by a filtering mechanism, *Circ. Res.* **25**, 39 (1969).
- [54] I. V. Pivkin and G. E. Karniadakis, Accurate Coarse-Grained Modeling of Red Blood Cells, *Phys. Rev. Lett.* **101**, 118105 (2008).
- [55] D. A. Fedosov, B. Caswell, and G. E. Karniadakis, A multiscale red blood cell model with accurate mechanics, rheology, and dynamics, *Biophys. J.* **98**, 2215 (2010).
- [56] M. Dao, J. Li, and S. Suresh, Molecularly based analysis of deformation of spectrin network and human erythrocyte, *Mater. Sci. Eng., C* **26**, 1232 (2006).
- [57] P. Español, Fluid particle model, *Phys. Rev. E* **57**, 2930 (1998).
- [58] M. B. Liu, G. R. Liu, L. W. Zhou, and J. Z. Chang, Dissipative particle dynamics (dpd): An overview and recent developments, *Arch. Comput. Methods Eng.* **22**, 529 (2015).
- [59] See Supplemental Material at <http://link.aps.org/supplemental/10.1103/PhysRevFluids.8.063103> for (1) simulation results with different N_v , (2) definition of the increment of spectrin network connectivity, n , (3) DPD parameters.
- [60] S. Chien, K. L. Sung, R. Skalak, S. Usami, and A. Tözeren, Theoretical and experimental studies on viscoelastic properties of erythrocyte membrane, *Biophys. J.* **24**, 463 (1978).

- [61] J. P. Mills, L. Qie, M. Dao, C. T. Lim, and S. Suresh, Nonlinear elastic and viscoelastic deformation of the human red blood cell with optical tweezers, *Mol. Cell. Biomech.* **1**, 169 (2004).
- [62] R. M. Hochmuth and R. E. Waugh, Erythrocyte membrane elasticity and viscosity, *Annu. Rev. Physiol.* **49**, 209 (1987).
- [63] M. Dearnley, T. Chu, Y. Zhang, O. Looker, C. Huang, N. Klonis, J. Yeoman, S. Kenny, M. Arora, J. M. Osborne, R. Chandramohanadas, S. Zhang, M. W. Dixon, and L. Tilley, Reversible host cell remodeling underpins deformability changes in malaria parasite sexual blood stages, *Proc. Natl. Acad. Sci. USA* **113**, 4800 (2016).
- [64] G. Prado, A. Farutin, C. Misbah, and L. Bureau, Viscoelastic transient of confined red blood cells, *Biophys. J.* **108**, 2126 (2015).
- [65] R. Tran-Son-Tay, S. P. Sutera, and P. R. Rao, Determination of red blood cell membrane viscosity from rheoscopic observations of tank-treading motion, *Biophys. J.* **46**, 65 (1984).
- [66] T. Betz, M. Lenz, J. F. Joanny, and C. Sykes, ATP-dependent mechanics of red blood cells, *Proc. Natl. Acad. Sci. USA* **106**, 15320 (2009).
- [67] G. Deplaine, I. Safeukui, F. Jeddi, F. Lacoste, V. Brousse, S. Perrot, S. Biligui, M. Guillotte, C. Guitton, S. Dokmak *et al.*, The sensing of poorly deformable red blood cells by the human spleen can be mimicked in vitro, *Blood* **117**, e88 (2011).
- [68] T. Fujita, A scanning electron microscope study of the human spleen, *Arch. Histol. Jpn.* **37**, 187 (1974).
- [69] M. Dao, I. MacDonald, and R. Asaro, Erythrocyte flow through the interendothelial slits of the splenic venous sinus, *Biomech. Model. Mechanobiol.* **20**, 2227 (2021).
- [70] V. M. Turner and N. A. Mabbott, Influence of ageing on the microarchitecture of the spleen and lymph nodes, *Biogerontology* **18**, 723 (2017).
- [71] A. C. Groom, I. C. MacDonald, and E. E. Schmidt, Splenic microcirculatory blood flow and function with respect to red blood cells, in *The Complete Spleen* (Springer, 2002), pp. 23–50.
- [72] R. M. Hochmuth, Micropipette aspiration of living cells, *J. Biomech.* **33**, 15 (2000).
- [73] A. Matrai, R. Whittington, and E. Ernst, A simple method of estimating whole blood viscosity at standardized hematocrit, *Clin. Hemorheol. Microcirc.* **7**, 261 (1987).
- [74] M. L. Parks, R. B. Lehoucq, S. J. Plimpton, and S. A. Silling, Implementing peridynamics within a molecular dynamics code, *Comput. Phys. Commun.* **179**, 777 (2008).
- [75] E. A. Evans, R. Waugh, and L. Melnik, Elastic area compressibility modulus of red cell membrane, *Biophys. J.* **16**, 585 (1976).
- [76] T. Klei, R. Van Bruggen, J. Dalimot, M. Veldthuis, E. Mul, T. Rademakers, M. Hoogenboezem, S. Q. Nagelkerke, W. Van Ijcken, S.K. Moestrup, F. van Alphen, S. Meijer, T. Kuijpers, R. van Zwieten, and P. Svendsen, Hemolysis in the spleen drives erythrocyte turnover, *Blood* **134**, 946 (2019).